Supporting Information

Bifunctional Catalyst Directed Closed-Pore Engineering in Hard Carbon for enhanced sodium storage

Xiaoqi Yu[a], Xiaoyu Xu[a], Songyue Liu[a], Haiyan Liu[b], Hanyu Wei[a], Chengwei Fan[c], Ang Li[a], Xiaohong Chen[a], and Huaihe Song[a], *

a. State Key Laboratory of Chemical Resource Engineering, Beijing Key Laboratory of Electrochemical Process and Technology for Materials, Beijing University of Chemical Technology, Beijing 100029, P. R. China.

b. National Engineering Research Center of Coal Gasification and Coal-Based Advanced Materials, Shandong Energy Group CO., LTD, Jinan, P. R. China.

c. Xinjiang Institute of Engineering, Urumuqi 830023, P. R. China.

Xiaoqi Yu, E-mail: 2022400128@buct.edu.cn;

Xiaoyu Xu, E-mail: 2025400184@buct.edu.cn;

Songyue Liu, E-mail: 2023400130@buct.edu.cn;

Haiyan Liu, E-mail: xnylhy@shandong-energy.com;

Hanyu Wei, E-mail: 2023200471@buct.edu.cn;

Chengwei Fan, E-mail: fcw_upc@163.com;

Ang Li, E-mail: li_ang@mail.buct.edu.cn;

Xiaohong Chen, E-mail: chenxh@mail.buct.edu.cn;

Huaihe Song, E-mail: songhh@mail.buct.edu.cn;

Corresponding author email address

Fax: +86- 10- 6443-4916;

Tel: +86- 10- 6443-4916;

E-mail: songhh@mail.buct.edu.cn;

S1. Methods

S1.1 Materials Characterization

The chemical structure of the RF-0 and RF were characterized by ^{13}C CP/MAS solid-state NMR (Bruker AVANCE III 400 MHz). The TGA (Netzsch STA 449 F3) measurements were conducted from room temperature to 1500 °C at a heating rate of 10 °C min^{-1} under the argon atmosphere. The morphologies of the samples were characterized using field-emission scanning electron microscopy (FE-SEM, ZEISS SUPRATM 55). High-resolution transmission electron microscopy (HRTEM, Tecnai G2 F20 UTWIN) was employed to investigate lattice fringes and nanoscale ordering. Crystal structure was assessed via X-ray diffraction (XRD, Rigaku D/max2500B2+/PCX) with Cu Kα radiation (λ = 1.5406 Å), scanning from 10° to 90° (2θ). Raman spectra were acquired on a LabRAM Aramis (HORIBA Jobin Yvon) system with a 532 nm laser to evaluate graphitic domain characteristics. Chemical states and surface functional groups were analyzed by Fourier transform infrared spectroscopy (FTIR, Nicolet-iS50) and X-ray photoelectron spectroscopy (XPS, Thermo Scientific K-Alpha). Helium pycnometry (G-DenPyc 2900) was used to determine the true density of carbon materials at 25 °C. The specific surface area and pore characteristics were derived from N_2 adsorption-desorption isotherms measured with a Micromeritics ASAP 2020 instrument, with pore size distributions calculated based on density functional theory (DFT). The porosity was further probed by small-angle X-ray scattering (SAXS, Xuess2-0).

S1.2. Electrochemical Measurement

Electrode slurries were formulated via intensive homogenization of 80 wt% hard carbon (active material), 10 wt% sodium alginate (binder), and 10 wt% carbon black (conductive additive) in deionized water, which served as the dispersion medium. The homogenized slurry was then uniformly cast onto a copper foil current collector using a doctor-blade technique to form a thin film. The coated electrodes were dried under vacuum at 100 °C for 12 h to remove any residual moisture. For half-cell fabrication,

CR2032-type coin cells were assembled inside an argon-protected glove box (H_2O and O_2 levels < 0.1 ppm), employing metallic sodium as the counter/reference electrode, a glass fiber separator, and an electrolyte comprising 1 M $NaPF_6$ dissolved in a mixed solvent of ethylene carbonate and diethyl carbonate (EC/DEC, 1:1 by volume). Electrochemical cycling tests were carried out using a LAND CT2001 system between 0.001 and 2.8 V (vs. Na/Na^+) at ambient temperature. For full-cell evaluations, the RF-1100 anode was coupled with a $Na_3V_2(PO_4)_3$ (NVP) cathode with a controlled N/P capacity ratio ranging from 1.1 to 1.2. The NVP cathode was prepared by mixing NVP, carbon black, and Polyvinylidene fluoride (PVDF) in a weight ratio of 80:10:10 in N-methyl-2-pyrrolidone (NMP). The resulting homogeneous slurry was then cast onto aluminum foil using a doctor-blade. The coated NVP cathode was dried under vacuum at 100 °C for 12 h to remove any residual moisture. In addition, the RF-1100 anode was pre-sodiated by cycling for three cycles in a half-cell. These cells were tested within a voltage window of 1.5–3.7 V using the same EC/DEC-based electrolyte.

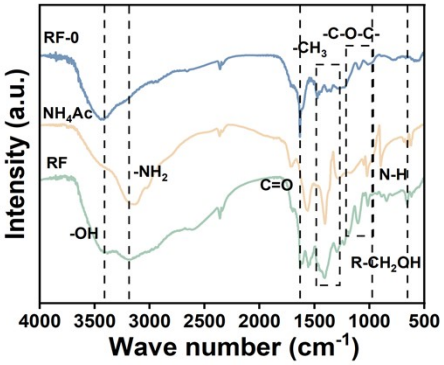

75

76 **Figure S1.** FTIR spectra.

77

Figure S2. Solid-state NMR shifts of RF-0 and RF.

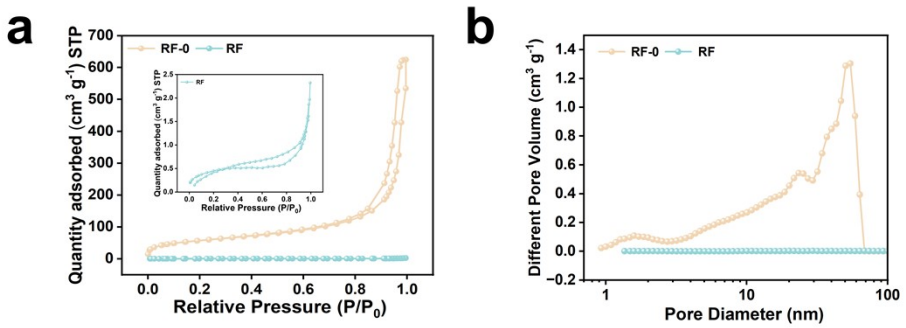

81

82 **Figure S3**. (a) N_2 adsorption−desorption isotherms, and (b) pore size distributions of

83 RF-0 and RF.

84

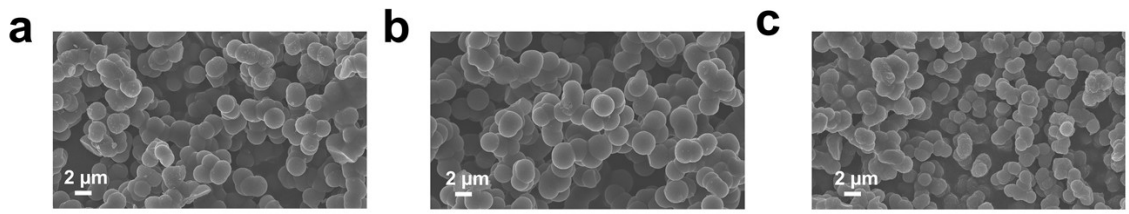

Figure S4. SEM images of (a) RF-1000, (b) RF-1100 and (c) RF-1300.

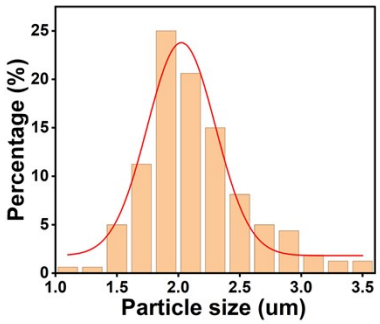

Figure S5. Particles size distribution image of RF-derived HC.

Figure S6. HRTEM images of (a) RF-1000, (b) RF-1100 and (c) RF-1300.

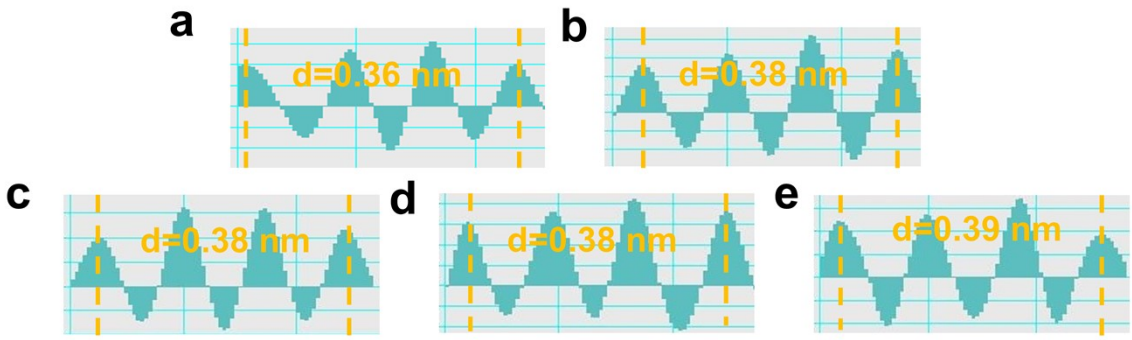

Figure S7. Interlayer spacings of (a) RF-0-1500, (b) RF-1500, (c) RF-1300, (d) RF-1100 and (e) RF-1000.

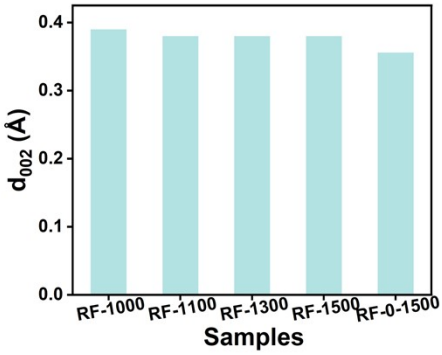

Figure S8. The values of d_{002} structural parameters.

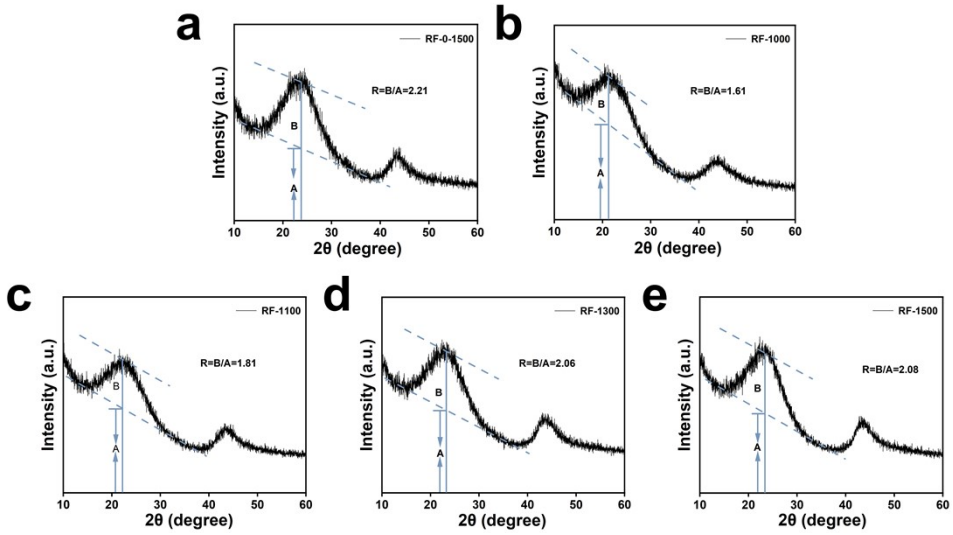

Figure S9. R values of (a) RF-0-1500, (b) RF-1000, (c) RF-1100, (d) RF-1300 and (e) RF-1500.

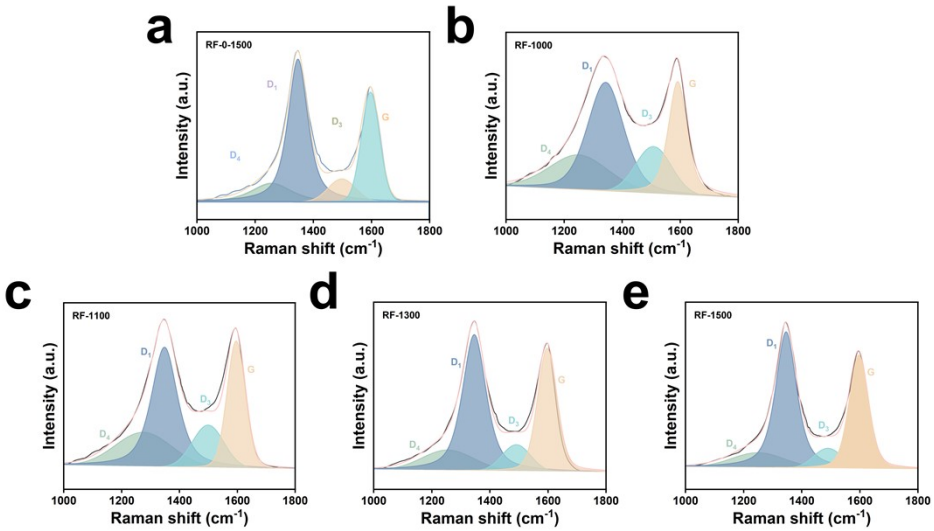

Figure S10. Peak fitting of the Raman spectra: (a) RF-0-1500, (b) RF-1000, (c) RF-1100, (d) RF-1300 and (e) RF-1500.

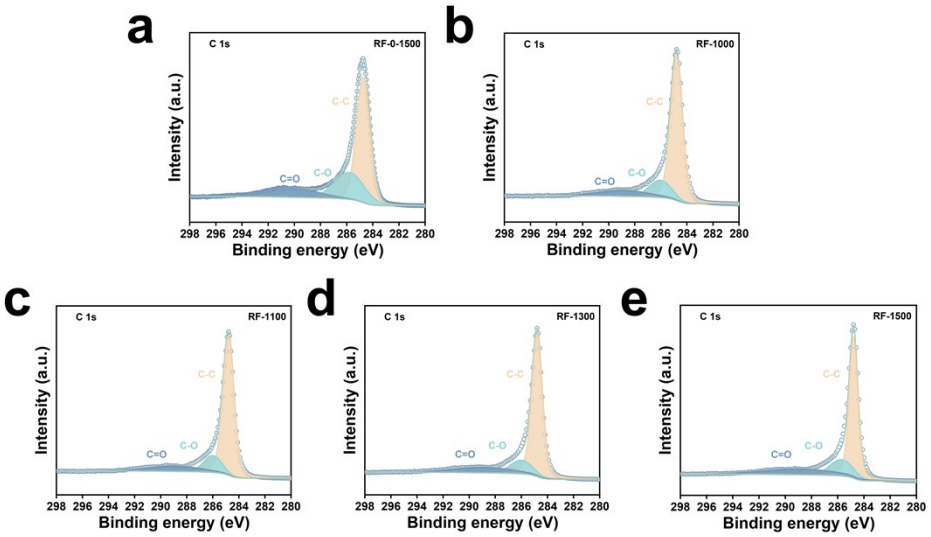

Figure S11. High-resolution C1s XPS spectra of (a) RF-0-1500, (b) RF-1000, and (c) RF-1100, (d) RF-1300 and (e) RF-1500.

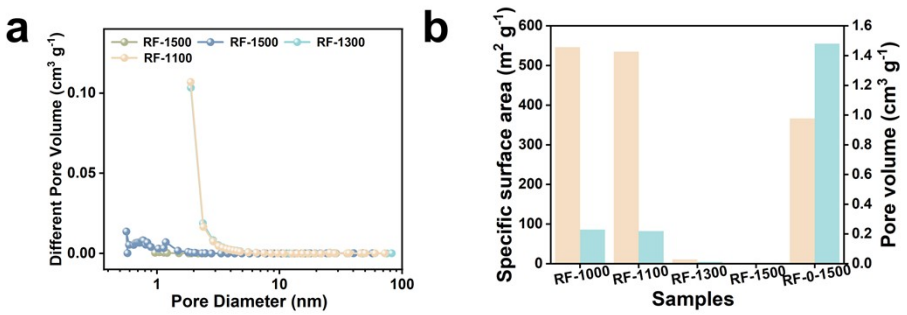

113

114 **Figure S12.** (a) Pore-size distributions of RF-1500, RF-1300, RF-1100 and RF-1000;

115 (b) BET specific surface area and pore volume for HCs.

116

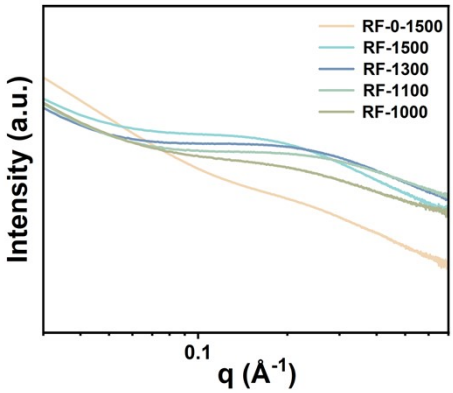

Figure S13. SAXS pattern of HCs.

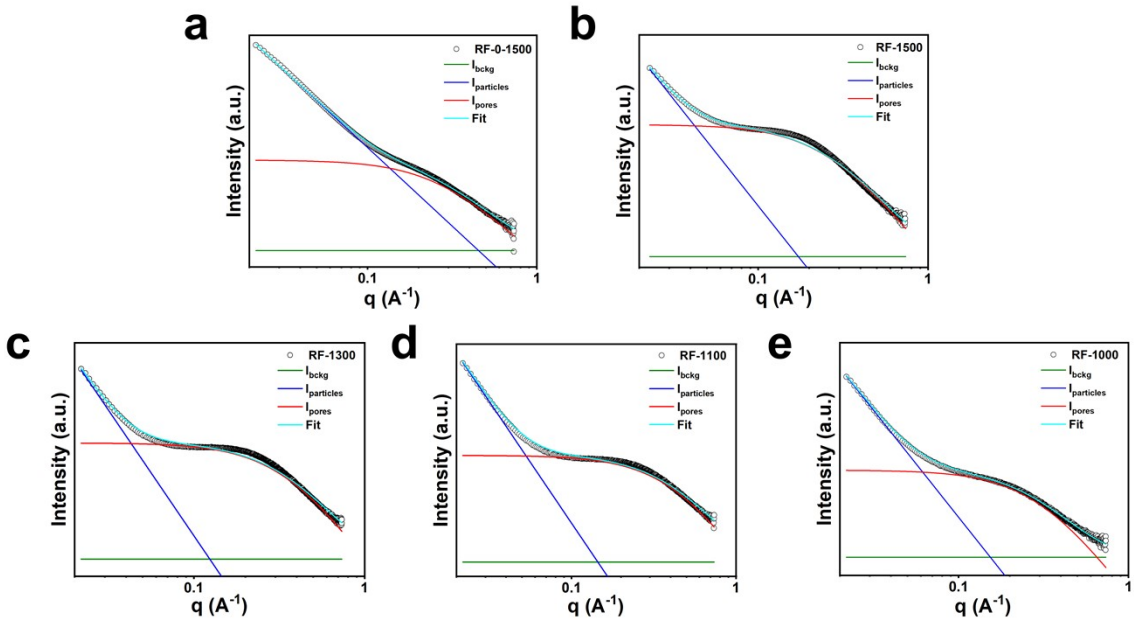

Figure S14. The fitted SXAS patterns of (a) RF-0-1500, (b) RF-1500, (c) RF-1300, (d) RF-1100 and RF-1000.

The scattering curves were deconvoluted into three components: a power-law region at low q values corresponding to the scattering from the entire hard carbon particles ($I_{particles}$), a hump in the q range of 0.1–0.5 $Å^{-1}$ associated with scattering from closed pores (I_{pores}), and a high-q background signal (I_{bckg}) arising from atomic-scale scattering. The fitting results based on the following model[1]:

$$I^{SAXS}(Q) = I_{particles}(Q) + I_{pores}(Q) + I_{bckg} \quad (1)$$

$$I_{particles}(Q) = \frac{A}{Q^k} \quad (2)$$

$$I_{bckg} = C \quad (3)$$

A is proportional to the total surface area of the large particles;

k the slope from Porod's law, reflecting interface roughness (k=4 indicates a smooth interface);

C is a constant

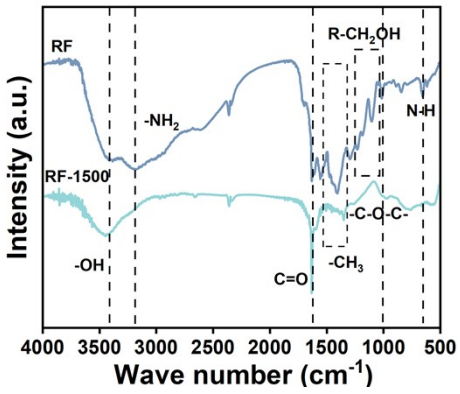

136

137 **Figure S15.** FTIR spectra of RF and RF-1500.

138

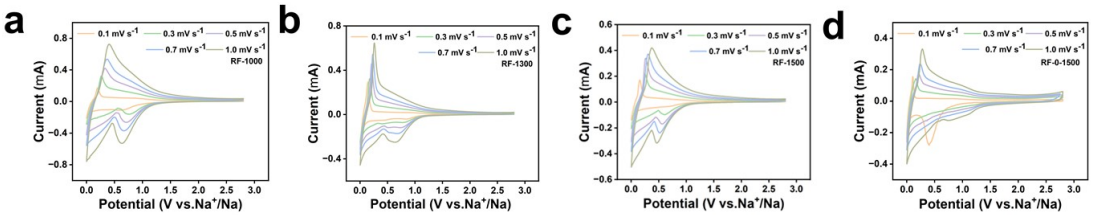

Figure S16. CV profiles of (a) RF-1000, (b) RF-1300, (c) RF-1500 and (d) RF-0-1500 at different scan rates from 0.1 to 1.0 mVs^{-1}.

The Na^+ storage mechanism in HCs is quantitatively analyzed using Equation 4:

$$i = av^b \quad (4)$$

where i is the current density and v is the scan rate. The exponent b-value close to 0.5 indicates that the charge storage process is dominated by diffusion control, while the b-value approaching 1.0 signifies that the process is primarily governed by capacitive control [2, 3].

150

151 **Figure S17.** The calculated b values of (a) RF-1000, (b) RF-1300, (c) RF-1500 and (d)

152 RF-0-1500.

153

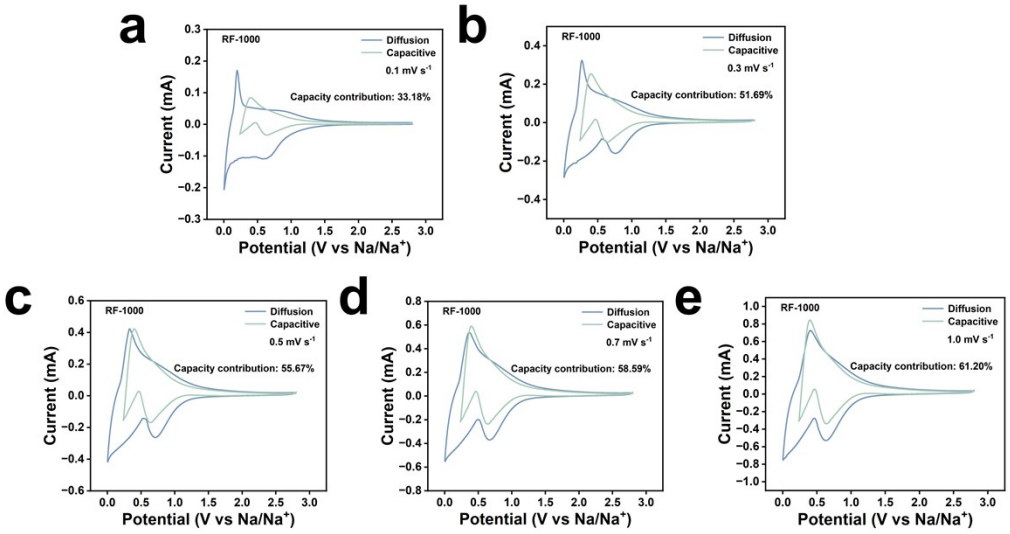

Figure S18. CV curves with calculated capacitive contribution for the RF-1000 anode at different scanning rates of (a) 0.1 mV s^{-1}, (b) 0.3 mV s^{-1}, (c) 0.5 mV s^{-1}, (d) 0.7 mV s^{-1}, and (e) 1.0 mV s^{-1}.

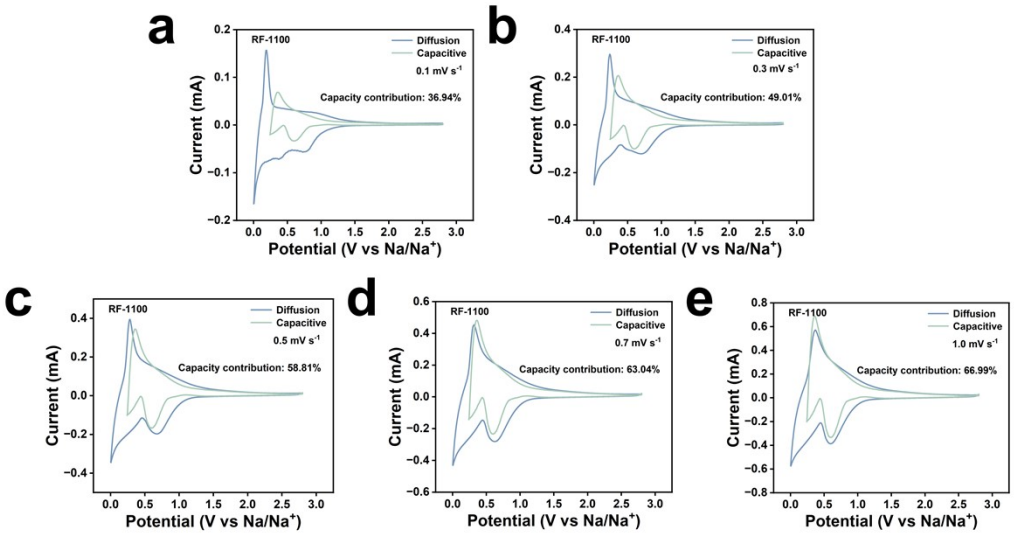

159

160 **Figure S19.** CV curves with calculated capacitive contribution for the RF-1100 anode

161 at different scanning rates of (a) 0.1 mV s^{-1}, (b) 0.3 mV s^{-1}, (c) 0.5 mV s^{-1}, (d) 0.7 mV

162 s^{-1}, and (e) 1.0 mV s^{-1}.

163

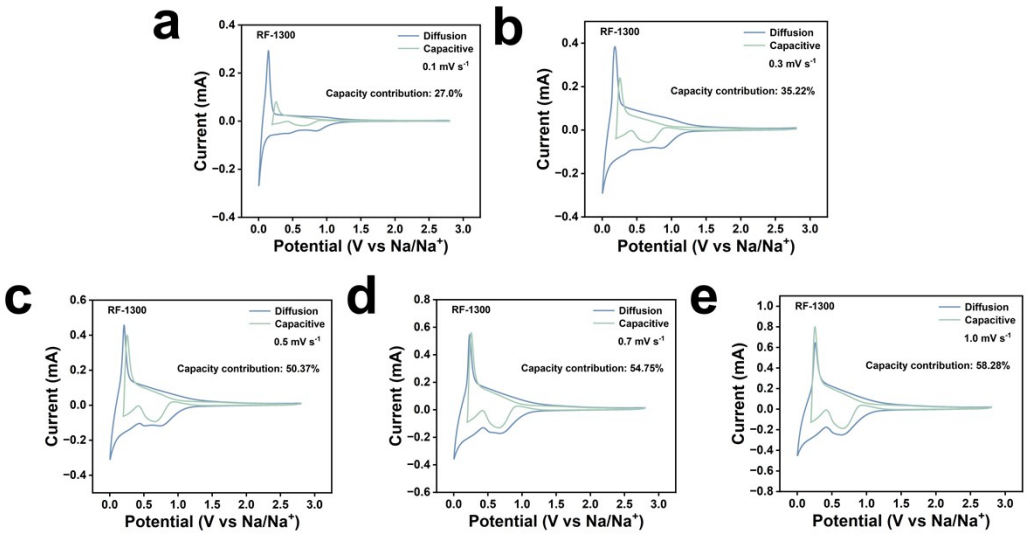

Figure S20. CV curves with calculated capacitive contribution for the RF-1300 anode at different scanning rates of (a) 0.1 mV s^{-1}, (b) 0.3 mV s^{-1}, (c) 0.5 mV s^{-1}, (d) 0.7 mV s^{-1}, and (e) 1.0 mV s^{-1}.

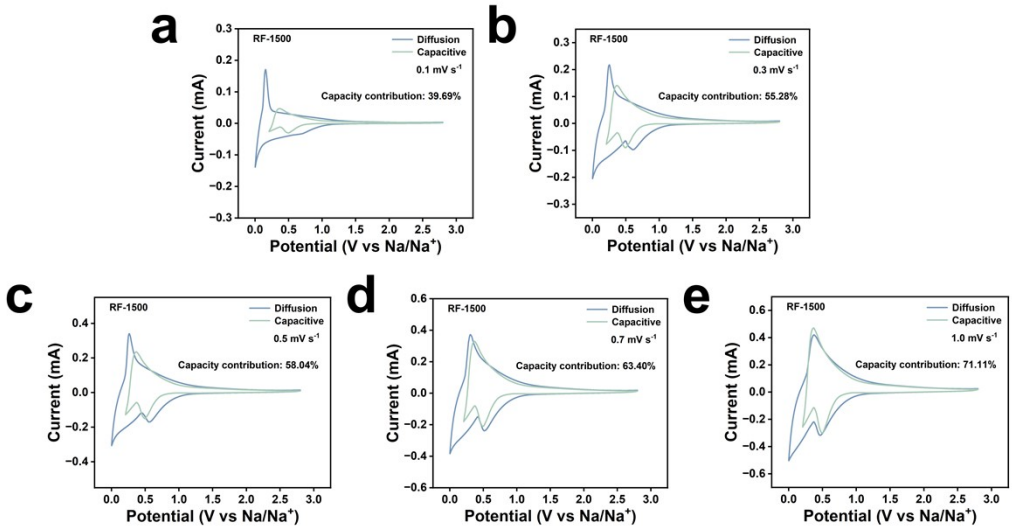

Figure S21. CV curves with calculated capacitive contribution for the RF-1500 anode at different scanning rates of (a) 0.1 mV s^{-1}, (b) 0.3 mV s^{-1}, (c) 0.5 mV s^{-1}, (d) 0.7 mV s^{-1}, and (e) 1.0 mV s^{-1}.

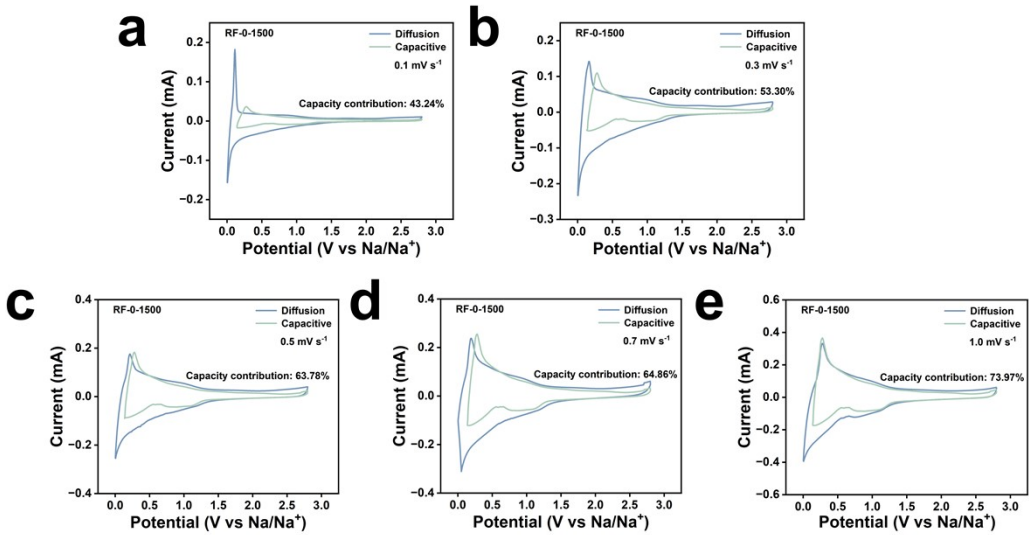

Figure S22. CV curves with calculated capacitive contribution for the RF-0-1500 anode at different scanning rates of (a) 0.1 mV s^{-1}, (b) 0.3 mV s^{-1}, (c) 0.5 mV s^{-1}, (d) 0.7 mV s^{-1}, and (e) 1.0 mV s^{-1}.

Furthermore, the current (i) at specific potentials can be quantitatively deconvoluted into capacitive-controlled contributions (proportional to k_1v) and diffusion-controlled contributions (proportional to $k_2v^{1/2}$) to quantify the relative contribution of each process to the total capacity [4, 5]. As expressed in Equation 5:

$$i = k_1 v + k_2 v^{\frac{1}{2}} \quad (5)$$

185 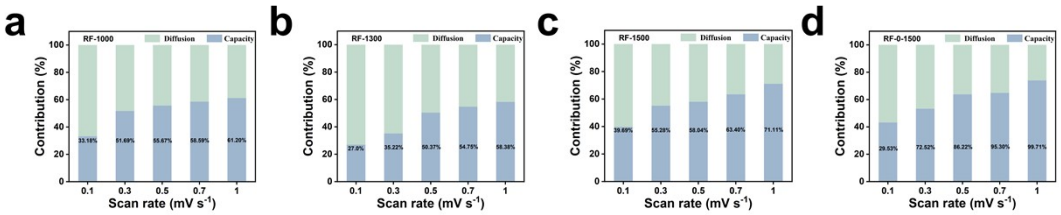

186 **Figure S23.** Percentage of diffusion-controlled and capacitive-controlled process of (a)
187 RF-1000, (b) RF-1300, (c) RF-1500 and RF-0-1500.
188

Table S1. Structural parameters for HCs.

Samples	d_{002} (nm)	La (nm)	Lc (nm)
RF-0-1500	0.36	5.66	1.43
RF-1500	0.38	4.18	1.07
RF-1300	0.38	3.88	1.02
RF-1100	0.38	3.79	1.04
RF-1000	0.39	3.1	0.95

Table S2. Deconvolution of O 1s XPS spectra showing contributions from C=O in HC samples.

Sample	C (%)	O (%)	C=O (%)
RF-1000	93.97	6.03	2.99
RF-1100	94.28	5.72	2.86
RF-1300	94.63	5.37	2.27
RF-1500	94.71	5.29	2.23
RF-0-1500	96.72	3.28	1.83

Table S3. The summarizing of the slope capacity and plateau capacity at different current densities for HCs.

Sample	Current densities (mA g^{-1})	Discharge capacity (mAh g^{-1})	Slope capacity (mAh g^{-1})	Plateau capacity (mAh g^{-1})
RF-1000	20	304.0	170.8	133.2
	50	253.0	144.2	108.8
	100	228.7	130.2	98.5
	200	193.9	117.0	76.9
	500	122.9	91.8	31.1
	800	101.6	80.0	21.6
	1000	93.8	66.8	27.0
	2000	76.3	33.5	42.8
RF-1100	20	432.2	144.4	287.8
	50	404.5	133.1	271.4

	100	371.3	118.3	253.0
	200	315.1	107.0	208.1
	500	134.4	91.8	42.6
	800	95.7	66.7	29.0
	1000	86.9	50.0	36.9
	2000	67.9	33.3	34.5
RF-1300	20	400.0	118.1	281.9
	50	336.6	100.8	235.8
	100	218.0	84.8	133.2
	200	102.4	70.0	32.4
	500	77.7	58.3	19.4
	800	68.22	40.0	28.2
	1000	63.6	33.3	30.3
	2000	51.1	33.5	17.6
RF-1500	20	398.2	107.0	291.2
	50	359.1	92.0	267.1
	100	272.3	81.0	191.3
	200	100.4	66.7	33.7
	500	65.5	50.0	15.5
	800	54.4	40.1	14.3
	1000	51.2	33.5	17.7
	2000	37.9	33.4	4.5
RF-0-1500	20	300.7	136.0	164.7
	50	166.0	101.0	65.0
	100	111.1	86.2	25.9
	200	97.1	76.5	20.6
	500	83.1	66.7	16.4
	800	76.5	53.3	23.2
	1000	73.6	49.9	23.7
	2000	63.8	33.3	30.5

Reference

[1] L. Kitsu Iglesias, E. N. Antonio, T. D. Martinez, L. Zhang, Z. Zhuo, S. J. Weigand, J. Guo, M. F. Toney, Revealing the Sodium Storage Mechanisms in Hard Carbon Pores, *Adv. Energy. Mater.*, 2023, **13**, 2302171.

[2] F. Wang, L. Chen, J. Wei, C. Diao, F. Li, C. Du, Z. Bai, Y. Zhang, O. I. Malyi, X. Chen, Y. Tang, X. Bao, Pushing slope- to plateau-type behavior in hard carbon for sodium-ion batteries via local structure rearrangement, *Energy Environ Sci.*, 2025, **18**, 4312-4323.

[3] M. Guo, H. Zhang, Z. Huang, W. Li, D. Zhang, C. Gao, F. Gao, P. He, J. Wang, W. Chen, X. Chen, M. Terrones, Y. Wang, Liquid Template Assisted Activation for "Egg Puff"-Like Hard Carbon toward High Sodium Storage Performance, *Small*. 2023, **19**, 2302583.

[4] B. Zhao, X. Li, L. Shang, C. Qiu, R. Yuan, H. Liu, T. Liu, A. Li, X. Chen, H. Song, Regulating oxygen functionalities of cellulose-derived hard carbon toward superior sodium storage, *J. Mater. Chem. A.*, 2024, **12**, 5834-5845.

[5] X. Xu, R. Yuan, C. Qiu, L. Guo, D. Zhang, Y. Cao, S. Lin, W. Yuan, Z. Zhang, A. Li, X. Chen, H. Song, Tailoring the Micronanostructure of Hard Carbon via Ball-Milling for Sodium-Ion Storage, *ACS Appl. Mater. Interfaces.*, 2025, **17**, 37907-37917.